LETTER

Structural properties of β-metal(II) hydroxides: Combined XAS and Raman spectroscopic studies on lattice stability

To cite this article: C. Marini *et al* 2018 *EPL* **122** 66002

epl A Letters Journal Exploring the Frontiers of Physics

June 2018

EPL, **122** (2018) 66002 www.epljournal.org
doi: 10.1209/0295-5075/122/66002

Structural properties of β-metal(II) hydroxides: Combined XAS and Raman spectroscopic studies on lattice stability

C. Marini[1(a)], W. Olszewski[1], N. Ramanan[1], B. Joseph[2], L. Simonelli[1] and P. Postorino[3]

[1] *ALBA Synchrotron, Cerdanyola del Vallès - 08290 Barcelona, Spain*
[2] *Elettra-Sincrotrone Trieste - S.S. 14-km 163,5, 34149 Basovizza, Trieste, Italy*
[3] *Dipartimento di Fisica, Università di Roma "Sapienza" - Piazzale Aldo Moro 2, 00185 Roma, Italy*

received 4 April 2018; accepted in final form 29 June 2018
published online 26 July 2018

PACS 61.05.cj – X-ray absorption spectroscopy: EXAFS, NEXAFS, XANES, etc.
PACS 65.40.-b – Thermal properties of crystalline solids
PACS 78.30.Er – Infrared and Raman spectra: Solid metals and alloys

Abstract – Temperature-dependent x-ray absorption (XAS) and high-pressure (HP) Raman spectroscopy results on two prominent β-metal(II) hydroxides, *viz.* β-$Ni(OH)_2$ and β-$Co(OH)_2$ are presented. Raman data at ambient conditions show the β-$Co(OH)_2$ phonons to be softer than the β-$Ni(OH)_2$ ones. Analysis of the extended x-ray absorption fine structure data at metal K-edge as a function of temperature reveals the Einstein frequencies of the metal-oxygen and the metal-metal bonds to be, respectively, 309 and 207 cm^{-1} for β-$Co(OH)_2$ and the same to be 385 and 240 cm^{-1} for β-$Ni(OH)_2$. In both the β-metal(II) hydroxides, up to about 10 GPa, HP Raman spectroscopy show a continuous hardening of the phonon modes associated with the metal-oxygen sub-lattices, whereas a systematic frequency softening is displayed by the hydroxyl symmetric stretching mode. These contrasting behaviours imply a gradual development of lattice instability with pressure mainly due to the displacement of H atoms around the metal-oxygen axis. The presented data allow a direct comparison of the local-lattice behaviour by quantifying the strength (XAS) and anharmonicity (RAMAN) of the atomic bonds in the two systems.

Introduction. – The simple structure of 3d metal oxides and hydroxides makes these compounds the ideal prototype for studying the stability of hydrous minerals with relevance to geophysical/geochemical phenomena [1]. Moreover, temperature- or pressure-dependent studies on hydroxides allow the more general understanding of the compression behaviour of hydrogen-containing materials [2]. Furthermore, these systems have been a subject of extensive research in the last decade due to their potential applications in photo-catalysis, energy storage and in electrochemical devices [3,4]. These compounds exist in two polymorphic forms, α and β [5,6], which are isostructural with hydrotalcite-like and brucite-like compounds, respectively. The active mass of several rechargeable alkaline batteries is constituted by the β forms of metal(II) hydroxides like $Ni(OH)_2$ and $Co(OH)_2$ [7,8]. A recent work demonstrated the high performance of electrochemical super-capacitors prepared from nickel hydroxide [9], graphene-cobalt hydroxide nanocomposites [10], and nickel-cobalt hydroxide nanosheets [11] due to their significantly improved electrochemical specific capacitance.

The β-$Ni(OH)_2$ and β-$Co(OH)_2$ exist in hexagonal symmetry with space group $P\bar{3}m1$ (number 164). The metal, oxygen and hydrogen atoms occupy positions (0, 0, 0), (1/3, 2/3, z) and (1/3, 2/3, u), respectively, where z and u are system-specific. Note that the metal occupies the Wyckoff position 1a and O and H occupy the Wyckoff position 2d [12,13]. The metal (M) atoms are sandwiched between two layers of oxygen atoms, resulting in an MO_6 octahedron. The OH bonds are oriented along the three-fold axis perpendicular to these layers. Previously, there have been several attempts to elucidate the structural and dynamical properties of these two β-metal(II) hydroxides using x-ray diffraction (XRD) [14–16], infrared and Raman spectroscopy [14,17–20] and neutron scattering [17,18,21–23]. Due to its unique ability to provide site-specific information about the local electronic and lattice structure (like oxidation state, coordination, numbers and identity of neighbours), x-ray absorption spectroscopy (XAS) provides direct information on atomic

(a) E-mail: cmarini@cells.es

bond strength and dynamics and is thus an ideal tool to characterize these compounds. In our recent work [24], we reported the local structural and electronic properties of β-$Ni(OH)_2$ deduced by a combined XAS and Raman spectroscopic investigation under high pressure (0–16 GPa). Our results revealed the onset of a weak structural/electronic instability in the high-pressure regime. In the present paper we extend our investigation to β-$Co(OH)_2$ and compare the results with that of β-$Ni(OH)_2$. We further use temperature-dependent (77–377 K) XAS data probing the local structure around the metal site of the two systems for further comparison. These data enable a direct comparison between the stability of the two β-metal(II) hydroxides on the basis of the inter-atomic distances and the related Debye-Waller factors, and the phonon frequencies.

Materials and experimental procedure. – For the temperature-dependent XAS measurements, commercial β-$Ni(OH)_2$ and β-$Co(OH)_2$ powders, from Sigma Aldrich, have been diluted in an inert matrix (BN) and pressed to a form of pellet. Transmission EXAFS measurements at Ni (8333 eV) and Co (7709 eV) K-edges were performed in q-EXAFS mode at the CLAESS beamline [25] of the Spanish National Light Source, (ALBA Synchrotron, Barcelona, Spain), using a Si 311 double-crystal monochromator. The incoming and outgoing photon fluxes were measured by ionization chambers filled with appropriate mixtures of N_2 and Kr gases. The sample was inserted into a liquid-nitrogen cryostat and the temperature was varied between 77 and 377 K, controlled by a feedback loop electric heater. For the pressure-dependent Raman measurements, pure powder of β-$Co(OH)_2$ has been compacted in the sample chamber of a membrane-driven diamond anvil cell (DAC), equipped with type-2A low-fluorescence diamonds. Since the bulk modulus of β-$Co(OH)_2$ is quite small (49 GPa, as reported in [14]), no hydrostatic medium has been used since the non-hydrostatic effect can be considered to be negligible. Raman spectra have been acquired by means of a confocal-microscope Raman spectrometer, equipped with a 20× objective, a 32 mW He-Ne laser (632.8 nm wavelength), and a 1800 lines/mm grating monochromator, coupled with a Peltier cooled CCD detector. Data have been collected in the backscattering geometry and a notch filter was used to reject the elastic contribution. The low-frequency cutoff of the notch filter limits the collection of reliable spectra below 130 cm^{-1}. Under these conditions, a few tens of micron diameter laser spot on the sample and a spectral resolution of about 3 cm^{-1} could be achieved. To complement these results, HP x-ray diffraction (HP-XRD) measurements [24] were carried out, using the Xpress beamline of the Elettra-Sincrotrone Trieste.

Results and discussion. –

Temperature-dependent XAS measurements. Temperature-dependent extended x-ray absorption fine structure (EXAFS) spectra and the corresponding Fourier transforms (FT) magnitudes for β-$Co(OH)_2$ and β-$Ni(OH)_2$, extracted from the respective metal K-edge XAS are presented in fig. 1 (panels (a), (b), (e) and (f)). The continuous Cauchy wavelet transform (CCWT) analysis method enables the visualization of the EXAFS spectra in three dimensions by decomposing the k-space and R-space signals [26]. Panels (c) and (d) of fig. 1 present the CCWT modulus at 77 K respectively for β-$Co(OH)_2$ and β-$Ni(OH)_2$. The visualized CCWT signals allow the identification of those local structural details which are difficult to be identified in a one-dimensional decomposition such as the Fourier transform of the EXAFS signal [27]. Peaks in the CCWT map can be identified by the theoretical calculation of $\chi(k)$ based on the structural parameters [12,13] using the FEFF8 code [28]. In both maps, the CCWT modulus presents three different structures. In each map, the intensities of these structures are quite different, simplifying the identification of scattering from heavy and light atom groups. The closest shape (appearing around 1.8 Å and centred around 6 $Å^{-1}$) is associated with the metal-OH octahedron (1st shell), whereas the second one (located at 2.7 Å and centred near 8 $Å^{-1}$) is due to the 6 next-nearest-neighbour metal atoms (2nd shell). Above this contribution, a region of positive and destructive interference is clearly visible; indicating the presence of

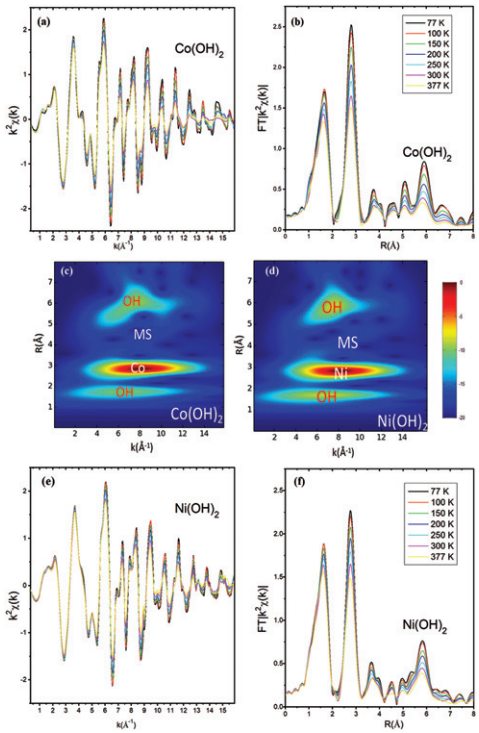

Fig. 1: (Colour online) Temperature dependence of the metal K-edge k^2-weighted EXAFS spectra ((a) and (e)) and the corresponding FT magnitudes ((b) and (f)) of the two β-metal(II) hydroxides. The corresponding continuous Cauchy wavelet transform modulus showing the localization of each EXAFS (O-H, Ni/Co atomic groups and MS (multiple-scattering)) contributions at 77 K is presented in (c) and (d).

Table 1: Results from EXAFS analysis on β-metal(II) hydroxides as a function of temperature.

Sample	T (K)	$R_{M\text{-}OH}$ (Å)	$R_{M\text{-}M}$ (Å)	$\sigma^2_{M\text{-}OH}$ (Å^{-2})	$\sigma^2_{M\text{-}M}$ (Å^{-2})
	77	2.094(4)	3.172(1)	0.0054(6)	0.0036(3)
	100	2.094(3)	3.172(4)	0.0054(6)	0.0039(3)
	150	2.095(4)	3.173(3)	0.0059(6)	0.0045(3)
β-Co(OH)$_2$	200	2.094(3)	3.173(4)	0.0065(6)	0.0052(3)
	250	2.095(4)	3.173(3)	0.0072(6)	0.0060(3)
	300	2.095(4)	3.174(3)	0.0080(6)	0.0068(4)
	350	2.096(4)	3.175(3)	0.0086(6)	0.0076(4)
	77	2.059(3)	3.116(3)	0.0041(6)	0.0039(3)
	100	2.061(2)	3.118(2)	0.0041(4)	0.0041(2)
	113	2.060(2)	3.118(2)	0.0042(4)	0.0040(2)
β-Ni(OH)$_2$	150	2.060(2)	3.120(2)	0.0044(3)	0.0045(2)
	200	2.062(2)	3.121(2)	0.0047(3)	0.0049(2)
	250	2.062(2)	3.122(2)	0.0051(4)	0.0055(3)
	300	2.063(2)	3.122(2)	0.0056(4)	0.0061(3)
	373	2.064(3)	3.123(3)	0.0060(4)	0.0069(4)

counterphased multiple scattering signals. Finally, the weaker structure located around 6 Å and centred near 8 Å^{-1} represents a higher-order shell, originating from the single scattering signal from OH groups belonging to other octahedra. It is worth noticing that the signal is generally stronger in β-Co(OH)$_2$ than in β-Ni(OH)$_2$, thus suggesting that the structure of Co-hydroxide is more ordered than the Ni-one. HP-XRD data at the lowest pressure showing a narrower Bragg peak for β-Co(OH)$_2$ than for β-Ni(OH)$_2$ is in line with this.

The temperature increase causes a damping of the EXAFS oscillations due to the increase in the atomic thermal fluctuations, and this is reflected in the decrease in intensity of the FT peaks (fig. 1(b) and (f)). To obtain quantitative information from the measured data, EXAFS analysis has been performed [29] according to the standard equation:

$$\chi(k) = \sum_j \frac{N_j S_0^2}{kR_j^2} f_j\,(k, R_j.) \cdot e^{\frac{2R_j}{\lambda}} \cdot e^{2k^2\sigma_j^2} \sin\left(2kR_j + \delta_j(k)\right),$$

where R_j is the distance between the photoabsorber and the neighbouring j-atoms, N_j is the number of neighbouring atoms, S_0^2 is the passive electrons' amplitude reduction factor, $f_j(k, R_j)$ is the backscattered amplitude, λ is the photoelectron mean free path, $\delta_j(k)$ is the phase shift, and σ_j^2 is the correlated Debye-Waller (DW) factor measuring the mean square relative displacement (MSRD) between photoabsorber and backscatterer [30]. The EXAFS data were fitted using the Artemis program (version 0.9.20) of the IFFEFIT package [31]. In the model curve, $f_j(k, R_j)$, λ, and $\delta_j(k)$ were calculated using the FEFF-8 code [28].

We included only the first two shells: the first one corresponding to the OH backscattering and the second one associated with M-M scatter groups, for the EXAFS modelling to obtain reliable quantitative information. Recall that the maximum number of independent fitting parameters, n, is given by the formula $n = (2 \times \Delta k \times \Delta R)/\pi$, where Δk and ΔR are the windows used in the fit. In the present study $\Delta k = 14$ Å^{-1} and $\Delta R = 2.1$ Å, limiting the maximum number of free parameters to be ∼13. In order to minimize n, we kept all the coordination numbers constant as obtained from the diffraction data. Distances and Debye-Waller (DW) factors have been grouped. One distance and a corresponding DW factor have been fitted for each shell —the first shell taking into account the M-OH interaction and the second shell dealing with the M-M interaction. No multiple scattering paths were considered since their rank is relatively low compared to single scattering paths (see also CCWT maps). Finally, two other adjustable parameters (S_0^2 and E_0) have been introduced to account for the amplitude and common phase of the $\chi(k)$. The analysis results are summarized in table 1 and the DW factors for the M-OH group and M-M groups are plotted as a function of temperature in fig. 2.

The temperature evolution of the DW factors shows different slopes for the different bonds and systems, thus corresponding to different atomic bond strengths for M-OH and M-M in the two β-metal(II) hydroxides. In a temperature-dependent study it is possible to separate the static and dynamic DW factor contributions. In particular using the correlated Einstein model, the temperature-dependent Debye-Waller factor [32] can be fitted to

$$\sigma_j^2 = \sigma_{oj}^2 + \frac{\hbar}{2\mu_j \varpi_j^E} \coth\left(\frac{\hbar\varpi_j^E}{2K_B T}\right),$$

where μ_i is the reduced mass of the atomic pair and ω_{Ej} is the corresponding Einstein frequency. The best-fit curves are shown in fig. 2 along with the experimental points, while the fitted values are reported in table 2, together with the force constants calculated as the product $\mu_j \omega_{Ej}^2$.

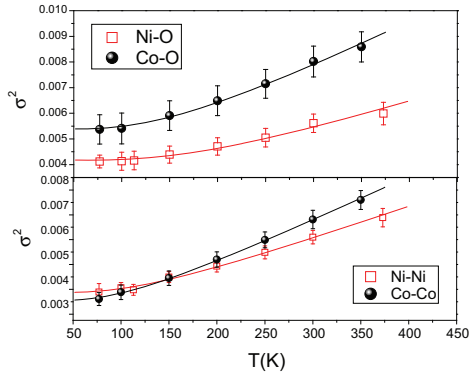

Fig. 2: (Colour online) DW factors (scatter points) for M-OH and M-M bounds in β-Ni(OH)$_2$ and β-Co(OH)$_2$, together with the correlated Einstein model (continuous lines) best fit curves.

Table 2: θ_E (K), ω_E (cm^{-1}), k, and σ_0^2 obtained from the correlated Einstein model fits of the EXAFS DW factors.

	Co-O	Co-Co	Ni-O	Ni-Ni
θ_E (K)	446(38)	298(29)	555(45)	346(34)
ω_E (cm^{-1})	309	207	385	240
k (eVÅ^{-1})	4.45	4.64	6.89	6.24
σ_0^2 (Å^{-2})	0.0054	0.0036	0.0042	0.0039

We observe that the static disorder, σ_0^2, is almost the same in the two β-metal(II) hydroxides for the M-M backscattering ($\sim$0.004 Å^{-2}), while it changes for the M-OH. Recall that the atomic masses of Co (58.933195(5) u) and Ni (58.6934(2) u) are very close. Passing from Co to Ni, the strength of the bonds (k) in the hydroxide strongly increases, most likely because of the difference in the electronic configuration of the absorber, which is indeed seen in the x-ray absorption near-edge structure (XANES) data shown in fig. 3(d). Note that the β-metal(II) hydroxides are isostructural and allow the same number and kind of phonon modes (see the following section).

Pressure-dependent Raman measurements. Raman spectra of β-Co(OH)$_2$ and β-Ni(OH)$_2$ after subtraction of the diamond fluorescence signal, are compared in fig. 3 at selected pressures. For both the samples, the group theory analysis of the zone-center phonon modes of brucite-type hydroxides demonstrates that the total irreducible representation is $\Gamma = 2A_{1g} + 3A_{2u} + 2E_g + 3E_u$. Four Raman active modes are allowed, three of which are lattice modes and one is a symmetric OH stretching vibration. According to the literature, the lowest-frequency lattice modes can be assigned to E_g (liberation) and A_{1g} (stretching), respectively. Higher-energy modes are associated with A_{2u} and E_g stretching and liberation of the M-O sublattice [14,20,24]. We note that the A_{2u} mode analysis is affected by the diamond fluorescence (see the shaded region in fig. 3(a)). The A_{1g} O-H internal stretching modes [14,20] are observed above 3000 cm^{-1} (see fig. 3(b)). While in β-Ni(OH)$_2$ a weak shoulder appears

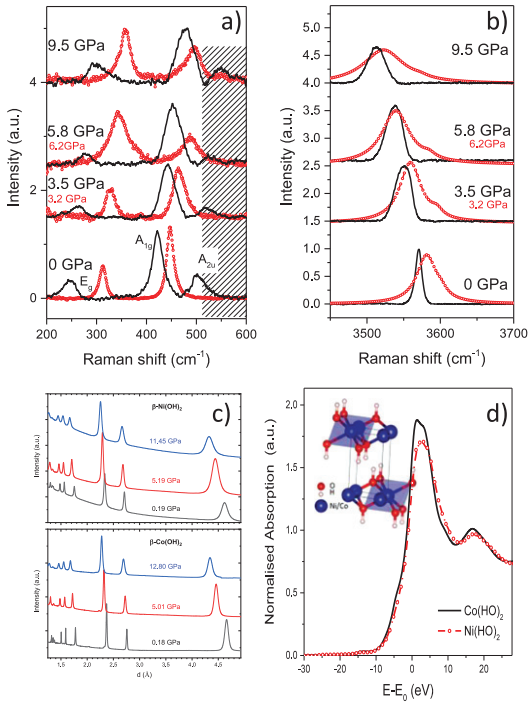

Fig. 3: (Colour online) Raman spectra ((a) and (b)) and XRD pattern (c) of β-Co(OH)$_2$ and β-Ni(OH)$_2$ at selected pressures. In (a) and (b) symbols correspond to β-Ni(OH)$_2$. In (a) the shaded region indicates the location of the most intense fluorescence feature from diamonds. (d) XANES spectra of the two β-metal(II) hydroxides at 77 K. To ease the comparison, the absorption edge of the two systems are set to zero. The inset in (d) shows a structural model of the β-metal(II) hydroxide.

on the high energy side, in β-Co(OH)$_2$, no shoulder of the main A_{1g} peak has been observed (see fig. 3(b)), consistent with earlier reports [14]. Although the two β-metal(II) hydroxides are isostructural, the strikingly larger FWHM of the A_{1g} O-H internal stretching mode at the lowest pressure indicates a varying local ordering consistent with the varying XANES features (edge and near-edge) observed at the metal K-edge in β-Co(OH)$_2$ and β-Ni(OH)$_2$. At ambient pressure as well as at higher pressures, the β-Co(OH)$_2$ phonons look generally softer than the β-Ni(OH)$_2$ ones. The ambient pressure case is in agreement with the EXAFS results (table 2).

No new phonon modes are observed in the Raman spectra of the β-Co(OH)$_2$ systems up to 10 GPa, indicating the absence of any evident structural phase transition, similarly to the β-Ni(OH)$_2$ case. This is indeed confirmed by the HP-XRD data (fig. 3(d)). With the application of pressure, a regular hardening of the low-energy phonon frequencies (related to M-O displacements) is observed (fig. 3(a)), while the high-frequency region shows a clear softening of the O-H internal stretching mode (fig. 3(b)). As a general feature, with an increase in pressure the Raman spectrum loses intensity and exhibits a considerable broadening of all the features. These findings can be interpreted as the result of an increase in disorder, which

Table 3: Calculated pressure slopes (dω/Dp) for Raman phonons modes of the two β-metal(II) hydroxides.

Sample	dω/dP(E_g) (cm^{-1}/GPa)	dω/dP (A_{1g}) (cm^{-1}/GPa)	dω/dP (A_{1g}(2)) (cm^{-1}/GPa)
β-Co(OH)$_2$	4.47 ± 2.44	5.25 ± 2.44	-5.99 ± 2.44
β-Ni(OH)$_2$ [24]	$4.76 +/2.44$	5.56 ± 2.44	-6.29 ± 2.44

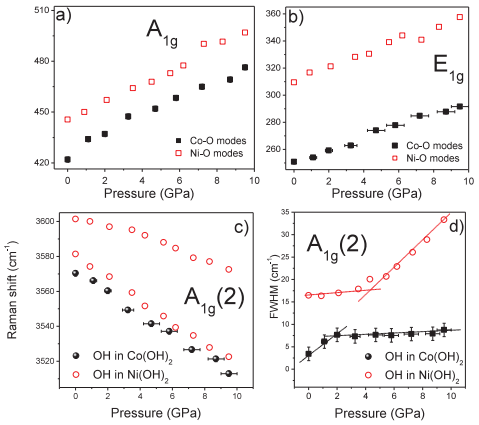

Fig. 4: (Colour online) β-Co(OH)$_2$ and β-Ni(OH)$_2$ (full and empty symbols, respectively) phonon frequencies (panels (a), (b) and (c)) and full width half-maximum (panel (d)) of E_g and A_{1g} modes as a function of pressure.

is further supported by the broadening of the diffraction peaks. To get quantitative information, the measured Raman spectra were fitted with a standard model curve [33] given by the sum of the phonon contributions, each described by a damped harmonic oscillator. Phonon frequencies (ω) and full width at half-maximum (FWHM) for β-Co(OH)$_2$ obtained using the described fitting procedure are shown in fig. 4, along with the corresponding values for β-Ni(OH)$_2$ taken from ref. [24]. The two hydroxides show very similar behaviour under pressure. However, a few subtle differences can be pinpointed. If we apply linear approximation to the pressure dependence of the phonon frequencies, we can calculate the slope as dω/dP. Values for dω/dP are reported in table 3.

Larger values of $|$dω/d$P|$ indicate a stronger anharmonicity of the phonon mode. We notice that the $|$dω/d$P|$ values for β-Ni(OH)$_2$ are higher than those for β-Co(OH)$_2$, *i.e.*, higher in the system characterized by stronger elastic constants of M-O and M-M atomic bonds (see table 2). The FWHM of the OH stretching peak (see fig. 4(d)) is seen to increase with a discontinuous pressure rate in both compounds. This result is in disagreement with recent investigations reported in [14], but it is consistent with previous spectroscopic studies [34,35], where the authors speculate about a "partial amorphization" of the OH sub-lattice. We observe that the threshold values (separating the two regimes observed in FWHM) occur at different pressures. For β-Co(OH)$_2$ and β-Ni(OH)$_2$ these values are found to be around 2 and 4–5 GPa, respectively. We remark that higher pressure values (at which the anomaly occurs) are found in the compound characterized by stronger elastic constants (*i.e.*, in Ni(OH)$_2$). The observed findings suggest the presence of a nonlinear mechanism of disorder of the O-H bonds in the two hydroxides as a result of lattice compression.

Conclusions. – In conclusion, we have presented a temperature-dependent x-ray absorption spectroscopy study of β-M-hydroxide (M = Co, Ni) together with a pressure-dependent Raman spectroscopic investigation over the same systems. The metal K-edge EXAFS analysis has allowed for the characterization of the local environment around the absorber atom. Distances, DW factors and elastic constants for both M-O and M-M atomic bonds have been calculated. Raman spectra collected at ambient condition confirm general softer bonds for the β-Co(OH)$_2$ once compared with the β-Ni(OH)$_2$ compound. High-pressure Raman investigation of the phonon spectra of β-Co(OH)$_2$ has been compared with the previously published results for β-Ni(OH)$_2$ [24]. In both cases, while the M-O vibrations experience a hardening of the phonon modes, the hydroxyl stretch mode shows a linear softening. However, the lattice response is different for the two systems, which are characterized by a different anharmonicity that appears indirectly proportional to the estimated lattice constants from the temperature-dependent XAS study. Moreover, the FWHM of the high-energy mode increases at a discontinuous rate with a threshold pressure close to 2 and 4–5 GPa for β-Co(OH)$_2$ and β-Ni(OH)$_2$, respectively. Overall, the Raman results suggest that the M-O sublattices remain essentially intact as a function of pressure though some minor anomalies occur as indicated by a progressive broadening (*i.e.*, pressure increases probably only the static disorder of the systems); while the H sublattice undergoes some subtle structural rearrangement. We believe this anomalous behaviour is related to the intrinsic local properties, and in particular to the different local bond force strengths detected in the β-Co(OH)$_2$ and β-Ni(OH)$_2$ systems.

* * *

One of us (BJ) acknowledges the IISc-ICTP fellowship from IISc Bangalore and ICTP Trieste.

REFERENCES

[1] Parise J. B., Leinenweber K., Weidner D. J., Tan K. and Von Dreele R. B., *Am. Mineral*, **79** (1964) 193.
[2] Zttel A., *Mater. Today*, **6** (2003) 24.

[3] Zhang J., Zhang L., Liu H., Sun A. and Liu Rushi, *Electrochemical Technologies for Energy Storage and Conversion* (Wiley, Singapore) 2012.

[4] Daniel C. and Besenhard J. O., *Handbook of Battery Materials* (Wiley, Weihneim) 2011.

[5] Liu Z., Ma R., Osada M., Takada K. and Sasaki T., *J. Am. Chem. Soc.*, **127** (2005) 13869.

[6] Oliva P., Leonardi J., Laurent J. F., Delmas C., Braconnier J. J., Figlarz M. and Fievet F., *J. Power Sources*, **8** (1982) 229.

[7] Zhu W. H., Zhu Y., Davis Z. and Tatarchuk B. J., *Appl. Energy*, **106** (2012) 307.

[8] Armstrong R. D. and Charles E. A., *J. Power Sources*, **25** (1989) 89.

[9] Lee J. W., Ahn T., Soundararajan D., Koc J. M. and Kim J. D., *Chem. Commun.*, **47** (2011) 6305.

[10] Chen S., Zhu J. and Wang X., *J. Phys. Chem. C*, **114** (2010) 11829.

[11] Huang L., Chen D., Ding Y., Feng S., Wang Z. L. and Liu M., *Nano Lett.*, **13** (2013) 3135.

[12] Xu Z. P. and Zeng H. C., *J. Mater. Chem.*, **8** (1998) 2499.

[13] Szytula A., Murasik A. and Balanda M., *Phys. Status Solidi B*, **43** (1971) 125.

[14] Shieh J. R. and Duffy T. S., *Phys. Rev. B*, **66** (2002) 134301.

[15] Garg N., Surinder S. K., Sharma M., Busseto E. and Sikka S. K., *Phys. B: Condens. Matter*, **349** (2004) 245.

[16] Zhen Z., Zhong X., Chen L., Ji Y. B. and Shen M., *Mater. Lett.*, **63** (2009) 1210.

[17] Bantignies J. L., Deabate S., Righi A., Rols S., Hermet P., Sauvajol J. L. and Henn F., *J. Phys. Chem.*, **112** (2008) 2193.

[18] Mockenhaupt C., Zeiskebc T. and Lutz H. D., *J. Mol. Struct.*, **443** (1998) 191.

[19] de Oliveira E. F. and Hase Y., *Vib. Spectrosc.*, **31** (2003) 19.

[20] Murli C., Sharma S. M., Kulshreshtha S. K. and Sikka S. K., *Phys. B: Condens. Matter*, **307** (2001) 111.

[21] Biendicho J. J., Roberts M., Norus D. and Lagerqvist U., *J. Mater. Res.*, **30** (2005) 407.

[22] Parise J. B., Loveday J. S., Nelmes R. J. and Kagi H., *Phys. Rev. Lett.*, **83** (1999) 328.

[23] Desgranges L., Calvarin G. and Chevrier G., *Acta Crystallogr. B*, **52** (1996) 82.

[24] Marini C., Joseph B., Caramazza S., Capitani F., Bendele M., Kantor I., Lotti P., Mathon O., Pascarelli S. and Postorino P., *High Press. Res.*, **37** (2017) 1.

[25] Simonelli L., Marini C., Olszewski W., vila Prez M., Ramanan N., Guilera G., Cuartero V. and Klementiev K., *Cogent Phys.*, **3** (2016) 1231987.

[26] Munoz M., Argoul P. and Farges F., *Am. Miner.*, **88** (2003) 694.

[27] Kim T., Song B., Lunt A. J. G., Cibin G., Dent A. J., Lu Li and Korsunsky A. M., *Chem. Mater.*, **28** (2016) 4191.

[28] Ankudinov A. L., Ravel B., Rehr J. J. and Conradson S. D., *Phys. Rev. B*, **58** (1998) 7565.

[29] Prins K., *X-ray Absorption: Principles, Applications, Techniques of EXAFS, SEXAFS, XANES* (Wiley, New York) 1988.

[30] Ravel B., *J. Synchrotron Radiat.*, **12** (2005) 537.

[31] Sevillano E., Meuth H. and Rehr J. J., *Phys. Rev. B*, **20** (1979) 4908.

[32] Joseph B., Iadecola A., Malavasi L. and Saini N. L., *J. Phys.: Condens. Matter*, **23** (2011) 265701.

[33] Congeduti A., Postorino P., Caramagno E., Nardone M., Kumar A. and Sarma D. D., *Phys. Rev. Lett.*, **86** (2001) 1251.

[34] Nguyen J. H., Kruger M. B. and Jeanloz R., *Phys. Rev. B*, **49** (1994) 3734.

[35] Nguyen J. H., Kruger M. B. and Jeanloz R., *Phys. Rev. Lett.*, **78** (1997) 1936.